□□□□□□□ □□ □□□□□□□□□□□ □□□□□	□□□□□□□ □□□□□□
□□□□□□	□□
□□□□□□	□□
□□□□ □□□□□	□□□□□□
□□□□	□□□□□□□□□
□□□	□□□□□□□□□□□□□□□□□□□□□□□□□□□□□□□□□□□□□□□

1

Extension of Operational Regime of LHD towards Deuterium Experiment

Y.Takeiri[1,2], T.Morisaki[1,2], M.Osakabe[1,2], M.Yokoyama[1,2], S.Sakakibara[1,2],
H.Takahashi[1,2], Y.Nakamura[1,2], T.Oishi[1,2], G.Motojima[1,2], S.Murakami[3],
K.Ito[1], A.Ejiri[4], S.Imagawa[1,2], S.Inagaki[5], M.Isobe[1,2], S.Kubo[1], S.Masamune[6],
T.Mito[1,2], I.Murakami[1,2], K.Nagaoka[1], K.Nagasaki[7], K.Nishimura[1], M.Sakamoto[8],
R.Sakamoto[1,2], T.Shimozuma[1], K.Shinohara[9], H.Sugama[1,2], K.Y.Watanabe[1],
J.W.Ahn[10], N.Akata[1,2], T.Akiyama[1], N.Ashikawa[1,2], J.Baldzuhn[11], T.Bando[2],
E.Bernard[12], F.Castejón[13], H.Chikaraishi[1], M.Emoto[1], T.Evans[14], N.Ezumi[15],
K.Fujii[16], H.Funaba[1], M.Goto[1,2], T.Goto[1,2], D.Gradic[11], Y.Gunsu[17], S.Hamaguchi[1],
H.Hasegawa[1,2], Y .Hayashi[6], C.Hidalgo[13], T.Higashiguchi[18], Y.Hirooka[1,2],
Y.Hishinuma[1], R.Horiuchi[1,2], K.Ichiguchi[1,2], K.Ida[1,2], T.Ido[1], H.Igami[1], K.Ikeda[1],
S.Ishiguro[1,2], R.Ishizaki[1], A.Ishizawa[19], A.Ito[1,2], Y.Ito[1], A.Iwamoto[1],
S.Kamio[1], K.Kamiya[9], O.Kaneko[20], R.Kanno[1,2], H.Kasahara[1], D.Kato[1,2], T.Kato[1],
K.Kawahata[1], G.Kawamura[1,2], M.Kisaki[1], S.Kitajima[21], W.H.Ko[22],
M.Kobayashi[1,2], S.Kobayashi[7], T.Kobayashi[1,2],
K.Koga[23], A.Kohyama[24], R.Kumazawa[1], J.H.Lee[22], D.López-Bruna[13],
R.Makino[1], S.Masuzaki[1], Y.Matsumoto[26], H.Matsuura[27], O.Mitarai,
H.Miura[1], J.Miyazawa[1,2], N.Mizuguchi[1], C.Moon[11], S.Morita[1,2], T.Moritaka[1],
K.Mukai[1,2], T.Muroga[1,2], S.Muto[1], T.Mutoh[28], T.Nagasaka[1,2], Y.Nagayama[1,2],
N.Nakajima[1], Y.Nakamura[19], H.Nakanishi[1,2], H.Nakano[1,2],
M.Nakata[1,2], Y.Narushima[1,2], D.Nishijima[29], A.Nishimura[1], S.Nishimura[1],
T.Nishitani[1], M.Nishiura[4], Y.Nobuta[26], H.Noto[1], M.Nunami[1,2],
T.Obana[1,2], K.Ogawa[1,2], S.Ohdachi[1,2], M.Ohno[2], N.Ohno[25], H.Ohtani[1,2],
M.Okamoto[30], Y.Oya[31], T.Ozaki[1], B.J.Peterson[1,2], M.Preynas[11],
S.Sagara[1,2], K.Saito[1], H.Sakaue[1], A.Sanpei[6], S.Satake[1,2], M.Sato[1],
T.Saze[1,2], O.Schmitz[32], R.Seki[1,2], T.Seki[1], I.Sharov[33], A.Shimizu[1], M.Shiratani[23],
M.Shohji[1], C.Skinner[10], R.Soga[25], T.Stange[11], C.Suzuki[1], Y.Suzuki[1,2],
S.Takada[1], K.Takahata[1,2], A.Takayama[1], S.Takayama[1], Y.Takemura[1,2],
Y.Takeuchi[34], H.Tamura[1], N.Tamura[1], H.Tanaka[25], K.Tanaka[1], M.Tanaka[1,2],
T.Tanaka[1,2], Y.Tanaka[35], S.Toda[1], Y.Todo[1,2], K.Toi[1], M.Toida[1], M.Tokitani[1,2],
T.Tokuzawa[1], H.Tsuchiya[1], T.Tsujimura[1], K.Tsumori[1,2], S.Usami[1,2], J.L.Velasco[13],
H.Wang[1], T.-H.Watanabe[36], T.Watanabe[37], J.Yagi[1,2], M.Yajima[1], H.Yamada[1,2],
I.Yamada[1], O.Yamagishi[1], N.Yamaguchi[38], Y.Yamamoto[1], N.Yanagi[1,2],
R.Yasuhara[1], E.Yatsuka[9], N.Yoshida[5], M.Yoshinuma[1,2], S.Yoshimura[1],
Y.Yoshimura[1]

[1]National Institute for Fusion Science, National Institutes of Natural Sciences, 322-6 Oroshi, Toki, Gifu 509-5368, Japan

[2]SOKENDAI, The Graduate University for Advanced Studies, 322-6 Oroshi, Toki, Gifu 509-5292, Japan

[3]Department of Nuclear Engineering, Kyoto University, Kyoto 606-8501, Japan

[4]Graduate School of Frontier Sciences, The University of Tokyo, 5-1-5 Kashiwanoha, Kashiwa-shi, Chiba-ken 277-8561, Japan

[5]Research Institute for Applied Mechanics, Kyushu University, 6-1 Kasuga-kouen, Kasuga, Fukuoka 816-8580, Japan

[6]Kyoto Institute of Technology, Matsugasaki, Sakyo-ku, Kyoto 606-8585, Japan

[7]Institute of Advanced Energy, Kyoto University, Kyoto 611-0011, Japan

[8]Plasma Research Center, University of Tsukuba, 1-1-1 Tennodai, Tsukuba, Ibaraki 305-8577, Japan

[9]National Institute of Quantum and Radiological Science and Technology, 801-1 Mukoyama, Naka-shi, Ibaraki 311-0193 Japan

[10]Oak Ridge National Laboratory, Oak Ridge, TN 37831, USA

[11]Max-Planck-Institut fuer Plasmaphysik, Wendelsteinstr.1, 17490 Greifswald, Germany

[12]Aix-Marseille Université, Jardin du Pharo 58, bd Charles Livon13284 Marseille Cedex 07, France

[13]Laboratorio Nacional de Fusion, Asociacion EURATOMCIEMAT, 28040 Madrid, Spain

[14]General Atomics, San Diego, CA, USA

[15]Nagano National College of Technology, 716 Tokuma, Nagano 381-8550, Japan

[16]Department of Mechanical Engineering and Science, Graduate School of Engineering, Kyoto University, Kyoto 606-8501, Japan

[17]POSTECH, Pohang, Gyeongbuk 790-784, Republic of Korea

[18]Department of Advanced Interdisciplinary Sciences, Center for Optical Research and Education (CORE), Utsunomiya University, 7-1-2 Yoto, Utsunomiya 321-8585, Japan

[19]Graduate School of Energy Science, Kyoto University, Kyoto 606-8501, Japan

[20]National Institutes of Natural Sciences, 4-3-13 Toranomon, Minato-ku, Tokyo 105-0001, Japan

[21]Department of Quantum Science and Energy Engineering, Tohoku University, Sendai 980-8579, Japan

[22]National Fusion Research Institute, 169-148 Gwahak-Ro, Yuseong-Gu, Daejeon 34133 Republic of Korea

[23]Department of Electronics, Kyushu University, 744 Motooka, Fukuoka 819-0395, Japan

[24]Organization of Advanced Sustainability Initiative for Energy System/Materials, Muroran Institute of Technology, Muroran, Hokkaido 050-8585, Japan

[25]Department of Energy Engineering and Science, Nagoya University, Furo-cho, Chikusa, Nagoya 464-8603, Japan

[26]Faculty of Engineering, Hokkaido University, Kita 13, Nishi 8, Kita-ku, Sapporo 060-8628, Japan

[27]Radiation Research Center, Osaka Prefecture University, 1-2 Gakuen-cho, Sakai Naka-ku, Osaka 599-8570, Japan

[28]Chubu University, 1200 Matsumoto-cho, Kasugai, Aichi 487-8501, Japan

[29]Center for Energy Research, University of California, San Diego, CA, USA

[30]Ishikawa National College of Technology, Kitachujo, Tsubata, Ishikawa 929-0392, Japan

[31]Radioscience Research Laboratory, Faculty of Science, Shizuoka University, 836 Oya, Suruga-ku, Shizuoka 422-8529, Japan

[32]Department of Engineering Physics, University of Wisconsin-Madison 1500 Engineering Drive Madison, WI 53706, USA

[33]St. Petersburg State PolyTechnical University, 29 Politechnicheskaya, St.Petersburg 195251, Russia

[34]Department of Information Systems, Daido University, 10-3 Takiharu-cho, Minami-ku, Nagoya 457-8530, Japan

[35]Division of Electrical Engineering and Computer Science, Kanazawa University, Kakuma, Kanazawa 920-1192, Japan

[36]Department of Physics, Nagoya University, Furo-cho, Chikusa, Nagoya 464-8602, Japan

[37]SOLAR-C Project Office, The National Astronomical Observatory of Japan, 2-21-1 Osawa, Mitaka, Tokyo 181-8588, Japan

[38]Physics Laboratory, Graduate School of Medicine and Pharmaceutical Sciences, University of Toyama, Toyama 930-0194, Japan

E-mail contact of main author: takeiri@nifs.ac.jp

Abstract. As the finalization of the hydrogen experiment towards the deuterium phase, the exploration of the best performance of the hydrogen plasma was intensively performed in the Large Helical Device (LHD). High ion and electron temperatures, T_i, T_e, of more than 6 keV were simultaneously achieved by superimposing the high power electron cyclotron resonance heating (ECH) on the neutral beam injection (NBI) heated plasma. Although flattening of the ion temperature profile in the core region was observed during the discharges, one could avoid the degradation by increasing the electron density. Another key parameter to present plasma performance is an averaged beta value $<\beta>$. The high $<\beta>$ regime around 4 % was extended to an order of magnitude lower than the earlier collisional regime. Impurity behaviour in hydrogen discharges with NBI heating was also classified with the wide range of edge plasma parameters. Existence of no impurity accumulation regime where the high performance plasma is maintained with high power heating > 10 MW was identified. Wide parameter scan experiments suggest that the toroidal rotation and the turbulence are the candidates for expelling impurities from the core region.

1. Introduction

The final goal of the LHD project is to obtain the high performance helical plasma relevant to the fusion reactor, i.e., $T_i > 10$ keV, $<\beta> > 5$ %, $n_e \tau_E T_i > 10^{20}$ keVm^{-3}s, and long pulse length of more than 3600 s with heating power of 3 MW [1]. With great efforts and contributions not only from domestic collaborators but also from all over the world, the LHD has produced many important results since the first plasma obtained in 1998. In particular, achievement of the high ion temperature plasma of 8.1 keV [2], super dense core mode (SDC) with central electron density of 1.2×10^{21} m^{-3} [3], high beta value of 5.1 % [4], and long pulse discharges of more than 48 minutes [5] are highly evaluated. Although these parameters have not been obtained simultaneously, each result is of the world record of non-tokamak magnetic fusion devices, which is the evidence that the LHD has led the stellarator/heliotron community as the world's largest superconducting net current free heliotron. Summary of the achieved parameters are presented in Table 1.

In addition to those achievements obtained by the continuous effort of optimization of plasma control and upgrading of the heating devices, some important discoveries and progress in plasma physics, plasma-wall interaction, and material science have been obtained. In

particular, featuring the heliotron configuration, the three-dimensional (3-D) effect on core and edge plasma transport was clearly demonstrated [6], and its mechanism could be explained by numerical simulation [7].

In order to achieve the final goal of the LHD, the deuterium experiment has started since March 2017. The deuterium plasma is expected to have better energy and particle confinement than the hydrogen plasma, which is clearly seen in tokamaks, but is not always obvious in helical devices. Thus it is worthwhile to see if such an isotope effect exists in helical plasmas or not. For this study, it is essential to know the marginal performance of the hydrogen plasma before the deuterium experiment starts. Intensive experiments were performed to expand the operational regime. In this paper, recent progress of the LHD experiment is overviewed, taking the forthcoming deuterium experiment into consideration.

TABLE 1. ACHIEVED PARAMETERS TOGETHER WITH THOSE TARGETS

Plasma parameters	Achieved		Target	
Ion temperature	8.1 keV	($n_e = 1 \times 10^{19} \text{m}^{-3}$)	10 keV	($n_e = 2 \times 10^{19} \text{m}^{-3}$)
Electron temperature	20 keV	($2 \times 10^{18} \text{m}^{-3}$)	10 keV	($2 \times 10^{19} \text{m}^{-3}$)
	10 keV	($1.6 \times 10^{19} \text{m}^{-3}$)		
Density	1.2×10^{21} m^{-3}	($T_e = 0.25$ keV)	$4 \times 10^{20} \text{m}^{-3}$	($T_e = 1.3$ keV)
Beta	5.1 %	($B_T = 0.425$ T)	5 %	($B_T = 1 - 2$ T)
	4.1 %	(1 T)		
Steady-state operation	54 min. 28 sec	(0.5MW, 1keV, $4 \times 10^{18} \text{m}^{-3}$)	1 hour	(3 MW)
	47min. 30sec.	(1.2MW, 2keV, $1 \times 10^{19} \text{m}^{-3}$)		

2. Experimental setup

The LHD is one of the largest superconducting helical devices, with poloidal/toroidal period numbers of 2/10, and major and averaged plasma minor radius of 3.6 – 4.0 m and 0.6 m, respectively [8]. Three negative-ion-based 180 keV neutral beams (NBI) with total heating power of ~ 16 MW are injected tangentially to generate and heat the plasma. It is available for these negative NBIs to be operated in the quasi steady-state mode, i.e., 10 minutes with 0.5 MW. Two positive-ion-based 40 keV NBs with total heating power of ~ 12 MW are also injected perpendicular to the plasma. For additional heating, ion cyclotron range of frequency heating (ICH) with total heating power of ~ 3 MW, and electron cyclotron resonance heating (ECH) with total heating power of ~ 5.4 MW are installed, and are sometimes utilized for the wall conditioning. The ECH can also be operated in the CW mode with 0.6 MW. For fuelling, the LHD is equipped with four gas puff valves and two frozen H_2 pellet injectors. With these facilities, hydrogen together with various impurity gases can be fed. The pellet injection can be varied from the single injection to the fast repetitive mode. Continuous injection can also be available.

Principal diagnostics in the LHD are routinely utilized in various experiments. The Thomson scattering system provides radial profiles of the electron temperature T_e and the electron

density n_e. The line averaged density is measured with the far infrared interferometer (FIR). Radiated power from impurities is measured with the bolometer array, and impurity densities with the charge exchange recombination spectroscopy system (CXRS). The visible and VUV spectroscopy systems are also employed to diagnose impurity ions and recycling particles. The plasma stored energy is measured with diamagnetic coils.

For the edge plasma control, the resonant magnetic perturbation (RMP) can be applied by using ten pairs of external coils installed on the up and the down sides of the torus.

3. Recent experimental results

3.1 High beta experiment

Production of the high beta plasma [9] is one of the most important issues in toroidal confinement systems to realize the economical fusion reactor. The LHD has explored the potential of stellarator/heliotrons to realize the high beta plasma. The beta value has increased every year with increasing the heating power. Optimization of magnetic configuration has also contributed to it.

Former high beta experiments were done in the low magnetic field of 0.425 T, which is in the low temperature, i.e., high collisional regime. To investigate the collisionality dependence of plasma confinement, high beta experiments with higher magnetic field of 1 T were performed, which realized higher electron temperature, i.e., lower collisionality. It is expected that the increase in the temperature raises the magnetic Reynolds number, S, which contributes to suppress the low-n resistive interchange mode.

History of the high beta experiment is shown in Fig. 1. Volume averaged beta value $<\beta>$ of more than 4 % was successfully obtained in an order lower collisional regime than that of the former experiment where the highest $<\beta>$ of 5.1 % was achieved [10]. Such a low collisional regime was realized by increasing the magnetic field up to 1 T, which produced the high temperature plasma. In this situation, transition to the improved particle confinement mode was observed when the $<\beta>$ increased. It is considered that the magnetic topology, especially in the edge region, was modified by the increase in $<\beta>$, stabilizing or destabilizing the MHD modes [11]. Spontaneous appearance of rational surfaces plays an important role. In order to realize the further extension of the plasma parameters to the reactor relevant regime, control of the edge magnetic topology to suppress the MHD instability is indispensable.
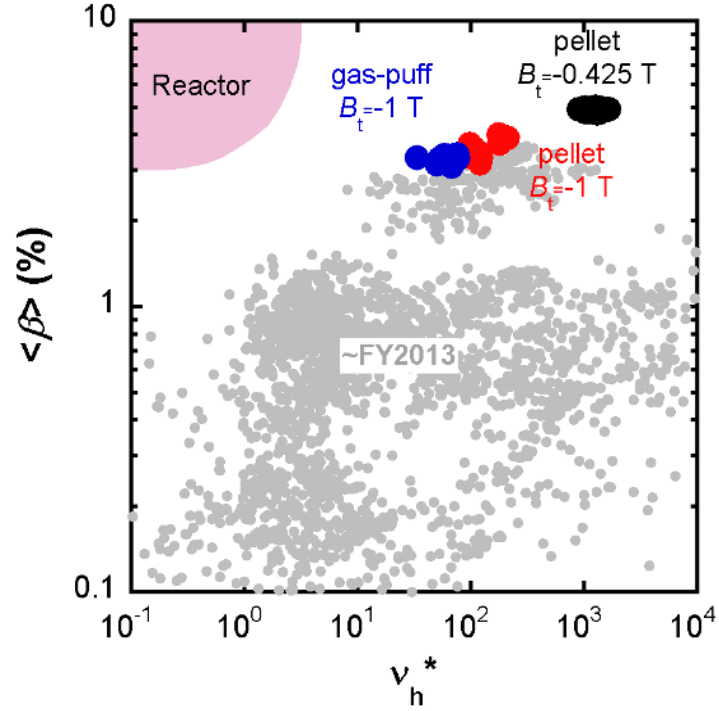
FIG. 1. Operational regime of averaged beta as a function of normalized collisionality.

3.2 Exploring high temperature regime

In LHD, each major plasma parameter, e.g., T_i, T_e, $<\beta>$ and n_e, has independently developed since the first plasma in 1998. In order to satisfy the reactor-relevant conditions, however, comprehensive progress is necessary. Recently, improvement of plasma heating devices and control techniques has led the LHD plasma to the advanced stage towards the reactor-relevant conditions [12].

In recent years, mega-watt-class 77 GHz and 154 GHz gyrotrons have been installed to increase T_e in the higher density regime. In the experiment, fine tuning of microwave launching was performed to optimize the power deposition on the appropriate resonant surface, using a newly developed ray-tracing code. This upgrade of the ECH scheme realized the efficient central heating, which resulted in the highest T_e of 10 keV with the formation of the electron internal transport barrier (e-ITB) in the relatively high averaged electron density regime of $\sim 2 \times 10^{19}$ m^{-3}. For the ion heating, improvement of the perpendicular NBIs and ICH antennas, together with the ICH wall conditioning technique, increased T_i up to 8.1 keV. The highest T_i and T_e mentioned above were obtained in different discharges [2]. On the other hand, in the burning plasma, where electron heating is dominant, T_i and T_e are expected to be comparable. Therefore, the experimental condition where T_i and T_e are simultaneously high is essentially required for future helical plasma studies. Superimposing the upgraded ECH on the NBI heated plasma, the ion internal transport barrier (i-ITB) and the e-ITB could simultaneously be formed in the high temperature plasma where both T_i and T_e, are more than 6.0 keV. Figure 2 shows the history of the operational regime of T_i and T_e. It is clearly shown that the operational regime was extended by the increase of the ECH power (green squares), and the optimization of the launching scheme (red circles) [13]. Note that most of the data

points in Fig.2 especially above 6 keV were obtained in the narrow density range between 1×10^{19} m^{-3} and 2×10^{19} m^{-3}.
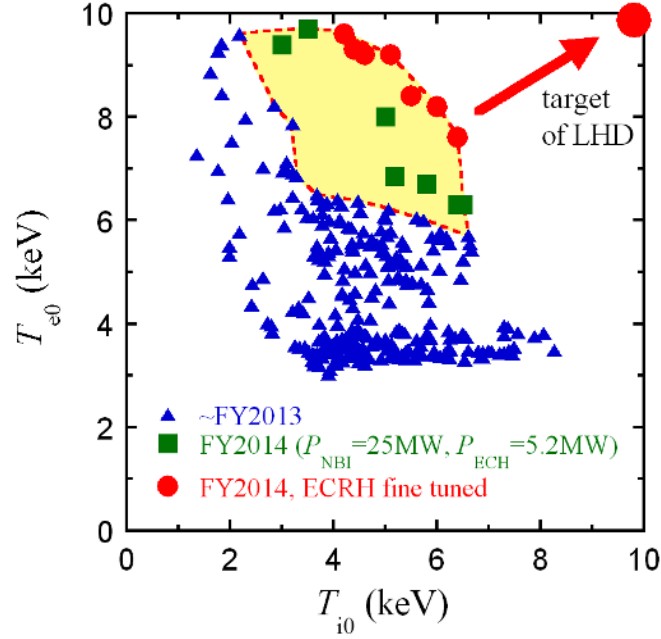

FIG. 2. History of operational regime of central electron and ion temperatures.

For the discharges with simultaneous achievement of high T_i and T_e, it is important to investigate the core/edge thermal transport. Figure 3 shows the time evolution of (a) port through power of NBI and ECH, (b) line-averaged-electron density, (c), (d) gradient of T_e and T_i at $r_{eff}/a_{99} = 0.31$ and 0.98, and (e) kinetic energy for electron and ion. On-axis ECRH was superposed stepwise up to ~5 MW on the NBI-sustained plasma. According to the ray trace calculation, more than 90% of ECRH power was absorbed inside $r_{eff}/a_{99} = 0.2$ at 4.74 s. It is found that T_e and its gradient increased with increase of ECRH power both in the plasma core and the edge. On the other hand, the T_i gradient decreased in the plasma core with increase in the ECRH power, as depicted in Fig. 3 (d).

However, core T_i can be increased by on-axis ECRH, if n_e is high, as is seen in Fig. 3 (i). This feature is quite beneficial for the high T_i scenario in high density plasmas such as DEMO, where electron heating is dominant.
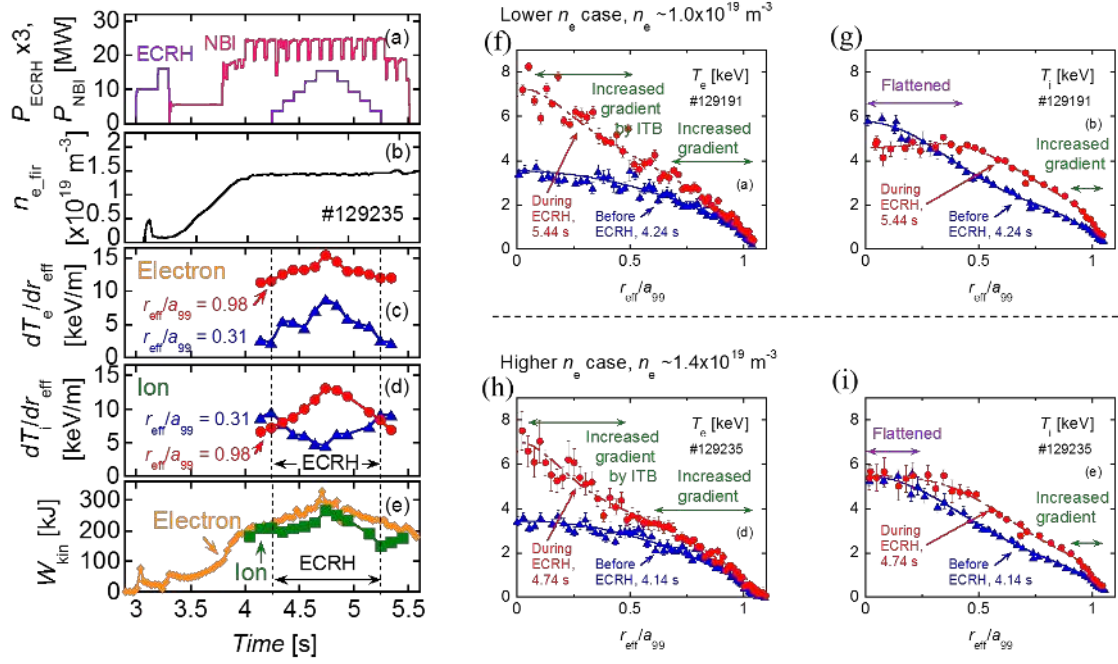
FIG. 3. Time evolution of (a) ECH and NBI power, (b) line averaged density, gradient of (c) electron temperature and (d) ion temperature and (e) kinetic energy for electron and ion. Radial profiles of electron and ion densities in (f), (g) low density case and (h), (i) high density case.

3.3 Impurity transport

In the high T_i and T_e, discharges shown in the previous subsection, it is typically observed that the carbon impurity is exhausted when high T_i and T_e are obtained with the formation of i-ITB and e-ITB. This phenomenon called "impurity hole" is not easy to understand because conventional modelling based on the neoclassical theory cannot simply explain the experimental result. That is, electric field is always negative and the direction of the impurity flux is "inward" with this experimental condition.

In order to understand such an unusual phenomenon, impurity behaviour in hydrogen discharges with NBI heating was classified, as shown in Fig. 4, with the plasma parameters (n_e, T_e) at the last closed flux surface (LCFS) [14]. In this classification, "accumulation" is evaluated as increase of core radiation ($dS_{rad}/dt > 0$). Physical studies on the critical condition at either side of the impurity accumulation window provide two different physical pictures based on neoclassical impurity transport in the core plasma and based on classical theory in the SOL region [15]. Impurity behaviour is generally dominated by the radial electric field (E_r) and impurity accumulation is always observed in the ion root with a large negative E_r (closed blue points). The dashed line is expressed by the constant ion collisionality with the same E_r value. Below the solid line, intrinsic impurities are shielded by friction force in the ergodic layer. The open red points indicate recent high power NBI discharges and impurity accumulation does not appear even in the region between two boundaries where impurity accumulation was expected. This suggests that there exists no impurity accumulation in high performance plasmas with high power heating ($P_{NBI} > 10$ MW) . This phenomenon is quite favourable for realizing fusion plasmas.
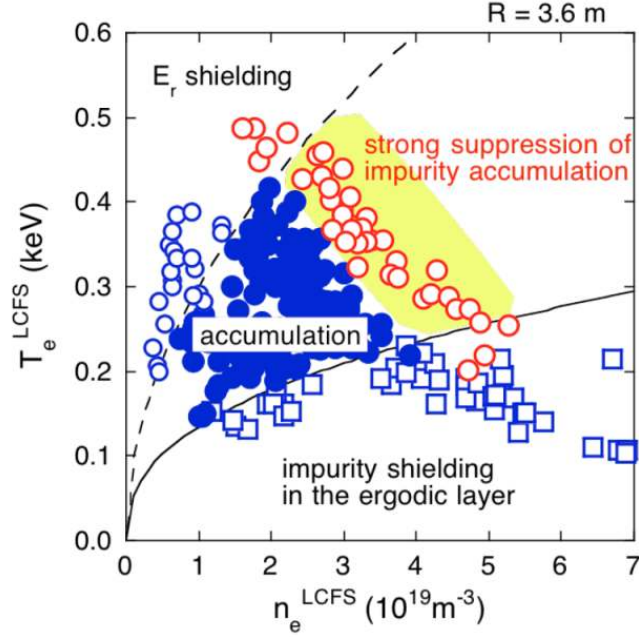
FIG. 4. n-T diagram at LCFS for impurity behavior. Closed and open blue symbols indicate low power discharges (P_{NBI} < 10 MW) with and without impurity accumulation, respectively. Open red points represent high power discharges (P_{NBI} = 13 MW) with the strong suppression of impurity accumulation.

The momentum transport experiment, together with the wide parameter scan experiment as shown in Fig. 4, suggests that the toroidal rotation plays an important role in the impurity behaviour, e.g., strong suppression of the impurity accumulation so-called "impurity hole". In addition, the high power discharge with net zero torque input (balanced NBI injection) shows the impact of ion temperature gradient on impurity transport. The carbon density profile becomes hollow with increasing the ion temperature gradient, which suggests that the ion temperature gradient also contributes to the strong outward convection in the suppression of impurity accumulation. Similar phenomena were observed in the W7-AS stellarator in its final experimental phase. After installation of the island divertor, W7-AS could gain the inherent density control up to 4×10^{20} m^{-3} and reach the high density H-mode (HDH) [16,17]. In HDH, the factor 2 increased energy confinement time was obtained with the factor 20 – 30 shorter impurity confinement time. The HDH suddenly occurred at the threshold density which increased with increasing the NBI power. Flushing out of the accumulated impurities from the core region was observed. In order to clarify the mechanism of the impurity hole observed in LHD, investigation of HDH results will be helpful.

As mentioned above, the bottom boundary of the impurity accumulation window in Fig. 4 is defined by the classical theory in the SOL region. In the SOL/edge region of the LHD, there exists an intrinsic stochastic layer, which strongly affects the balance between friction force and thermal force. Theoretical modelling with the EMC3/EIRENE code has clearly explained the impurity behaviour in the stochastic region [18], i.e., impurities from the divertor region are screened by the friction force in the high collisional regime.
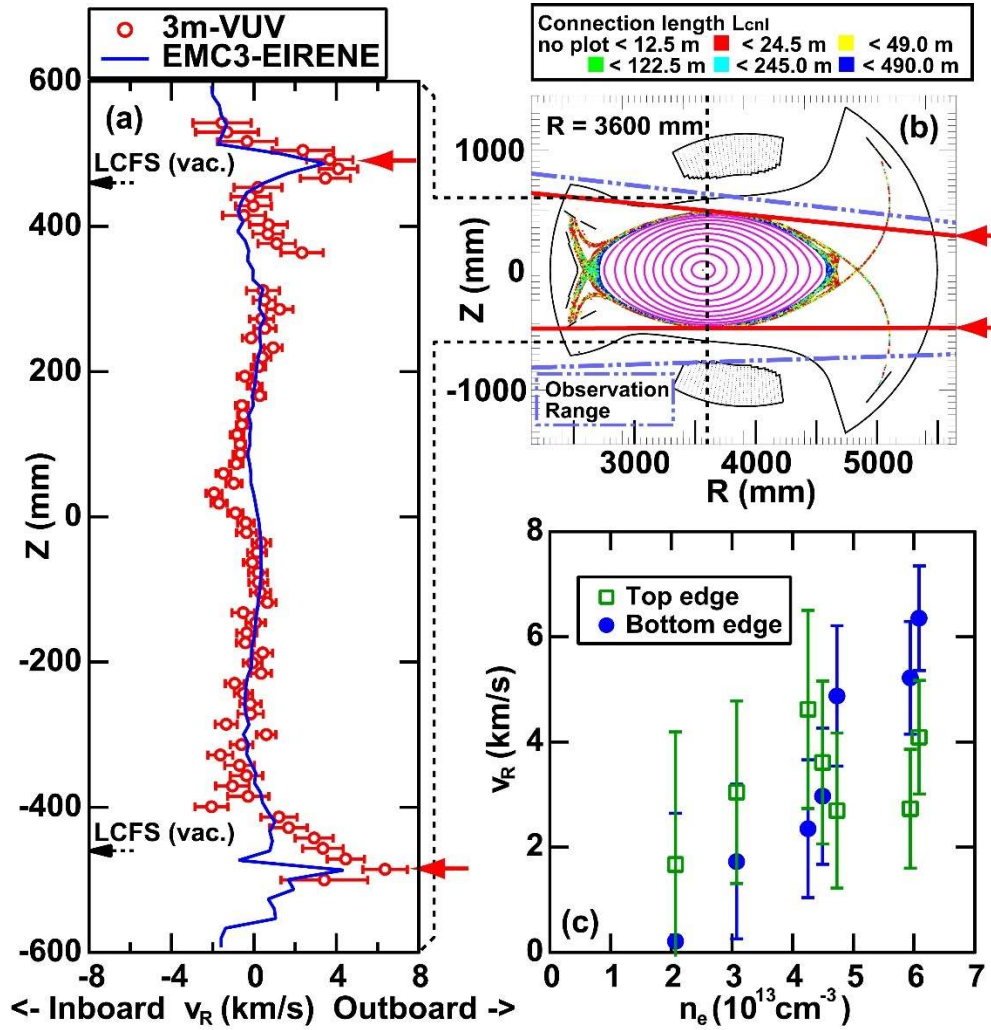
Fig. 5. (a) Vertical profile of C^{3+} impurity flow evaluated from Doppler shift of the second order of CIV line emission (2×1548.20 Å) measured by VUV spectroscopy. Synthetic profile of C^{3+} flow simulated with EMC3-EIRENE code is also plotted with solid line. (b) Observation range of the VUV spectroscopy. Two solid arrows in (a) correspond to each observation chord depicted with two solid arrows in (b). (c) Observed C^{3+} flow at the top and bottom edges of the stochastic layer as a function of density.

In order to verify the theoretical modelling, experimental and numerical results were compared for the hydrogen discharge of $R_{ax} = 3.6$ m, $B_t = 2.75$ T, $n_e = 6.0 \times 10^{19}$ m^{-3} and P_{NBI} = 10 MW [19]. Figure 5 (a) shows a full vertical profile of C3+ impurity flow evaluated from the Doppler shift of the second order of CIV line emission (2×1548.20 Å) at a horizontally-elongated plasma position of LHD. The observation range of the VUV spectroscopy [20] is also illustrated in Fig. 5 (b). Two arrows in Fig.5 (a) correspond to each observation chord depicted with two solid arrows in Fig.5 (b). Measured flow velocity in Fig. 5 (a) is a projection of the flow along the observation chord which can be approximately considered to be the direction of the plasma major radius. Figure 5 (c) shows the flow at the top and bottom edges of the stochastic layer as a function of density, indicating that the flow velocity increases with the density.

A synthetic profile of the simulated flow is depicted in Fig. 5 (a) with solid line, together with experimental result obtained by integrating the Doppler-shifted CIV intensities along the observation chord. Excellent agreement between experiment and simulation can be seen, which offers the conclusion that the parallel flow in the stochastic layer can be well explained by the presently used theoretical modelling on the edge impurity transport.

In conclusion, it can be said that the impurity parallel flow is mainly determined by the momentum balance along the magnetic field line. In particular, the friction force between impurity and bulk ions, and the ion thermal force driven by the ion temperature gradient are dominant terms in the momentum balance. The calculated friction force has the maximum value at the top and bottom edges of the stochastic layer where the impurity parallel flow also takes the maximum value. The impurity screening driven by the friction force is more effective in the higher electron density regime, as depicted in Fig. 5 (c).

3.4 Global particle balance during long pulse discharge

Exhausted particles through the stochastic region reach the divertor. As the final and then the first transport process for particles, the global particle balance (recycling process) should be clarified to achieve the steady-state operation for high performance plasma. History of the steady-state operation research is summarized in Fig. 6. Intensive efforts have been paid for realizing the steady-state operation [5], and the knowledge of the particle recycling in LHD has been accumulated.
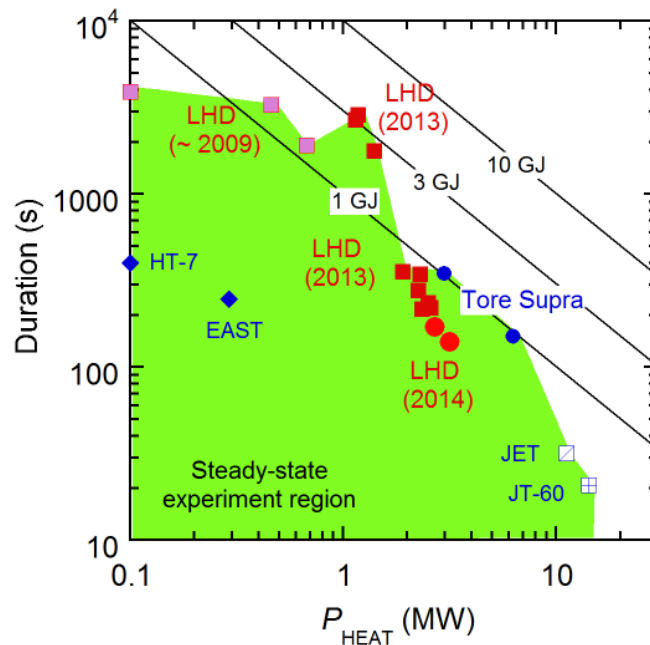

FIG. 6. History of steady-state operation research. Solid lines indicate launched energy.

In the LHD, the wall retention has been investigated for steady-state long pulse discharges [21,22]. As for the plasma facing components in LHD, stainless steel and graphite are employed for the first wall and divertor, respectively. The surface areas of the first wall and

the divertor plate are approximately 650 m² and 50 m², respectively. The first wall temperature is maintained below 370 K even in the baking for wall conditioning. The temperature on the surface divertor is approximately 500 K at maximum.
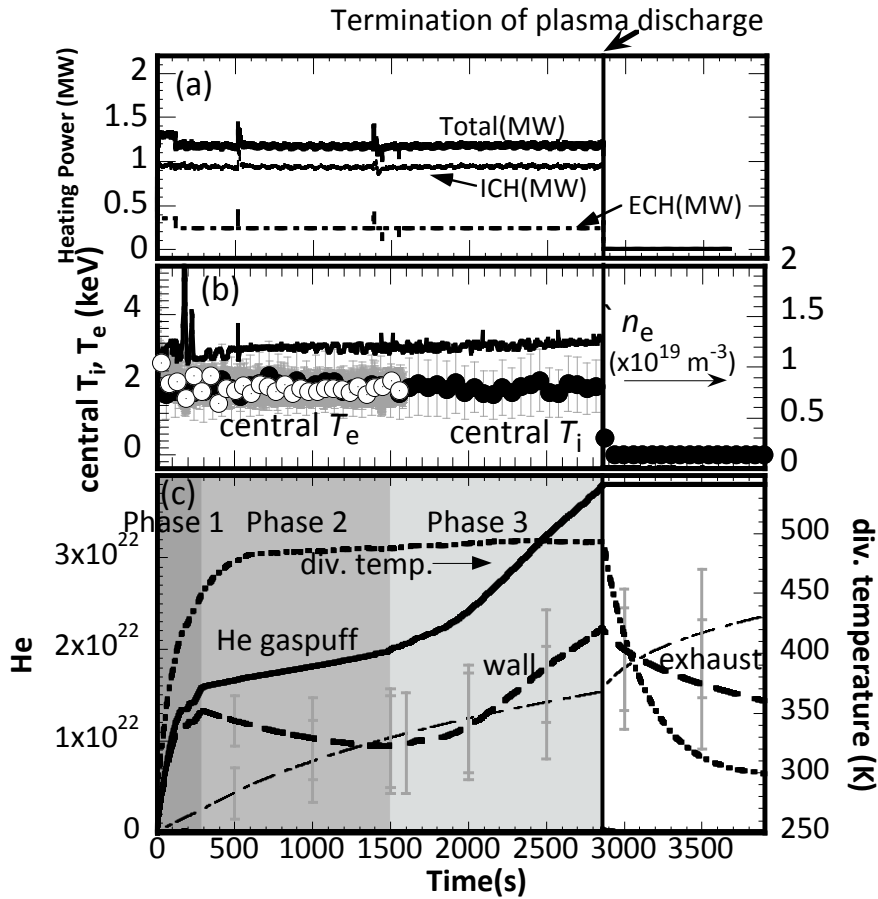

Fig. 7. Time evolution of (a) heating power for ICRH and ECH discharge and, (b) typical plasma parameters and (c) global helium particle balance analysis conducted in the long discharges.

Analysis of the global particle balance is conducted in the long-pulse helium discharge heated by ICH + ECH (1.2 MW × 48 min = 3.4×10³ MJ), as shown in Fig 7 (a). The heating energy injected into plasma is a new world record in toroidal plasmas [5]. A line-averaged electron density is 1.2×10^{19} m⁻³, and electron and ion temperatures of 2 keV are obtained as shown in Fig 7 (b). In the discharge, the global particle balance analysis was conducted. The gas balance analysis depends on the measurement of the injected and pumped particle fluxes during and after the plasma discharges. Therefore, identification of supplied and exhausted particles was undertaken carefully. The wall retention was evaluated by subtracting pumped particles from fed particles. Fig. 7 (c) shows the temporal evolution of the wall retention in the long pulse discharge. The dynamic change of the helium wall retention is observed. The inventory can be mainly separated into three phases. In the first phase, defined from 0 to 300 s, quite high wall inventory occurs. In this phase, more than 80% of the puffed helium is

retained in the wall. After the first phase, the wall inventory shows modest declination. However, the high wall inventory appears again in the third phase. The physics of the phased retention is discussed based on a simple assumption that there are two kinds of helium reservoir, "first wall with stainless" and "divertor plate with graphite".

4. LHD as the advanced academic platform

LHD has also been the platform for the advanced academic research to facilitate the high-temperature plasma physics and its contribution to wide-ranging academic fields.

The abrupt flow damping was found in LHD due to the magnetic stochastization induced by the change of the magnetic shear through the toroidal current control by means of switching Co- and Counter-NBIs [23]. Figure 8 (a) shows the radial profiles of the delay time of heat pulse produced by the modulated electron cyclotron heating (MECH) at three timings after switching the beam (at t=5.3 s). The topology of the magnetic field can be identified through the characteristics of the delay time [24] as the nested magnetic surfaces (t=5.75s), stochastic (t=6.25s) and magnetic island (t=6.73s), respectively. The central rotational transform measured by Motional Stark Effect spectroscopy (MSE) [25] increases, and the magnetic shear at the rational surface with $\iota/2\pi=0.5$ decreases during this period to reach the steady-state value of 0.5 at t=5.8s. The toroidal flow velocity measured by the charge exchange spectroscopy [26] is shown in Fig. 8 (b), where the abrupt damping of the toroidal flow at the central region is found associated with a transition from nested magnetic surfaces to a stochastic magnetic field. Physics mechanism for this abrupt flow damping has not been clarified, but candidates were proposed in Ref. [23], such as the change in the non-diffusive term of the toroidal momentum transport and the toroidal momentum pinch as a direct electromagnetic effect. This newly found breaking mechanism of the plasma flow associated with magnetic stochastization may also be relevant to astrophysics research.
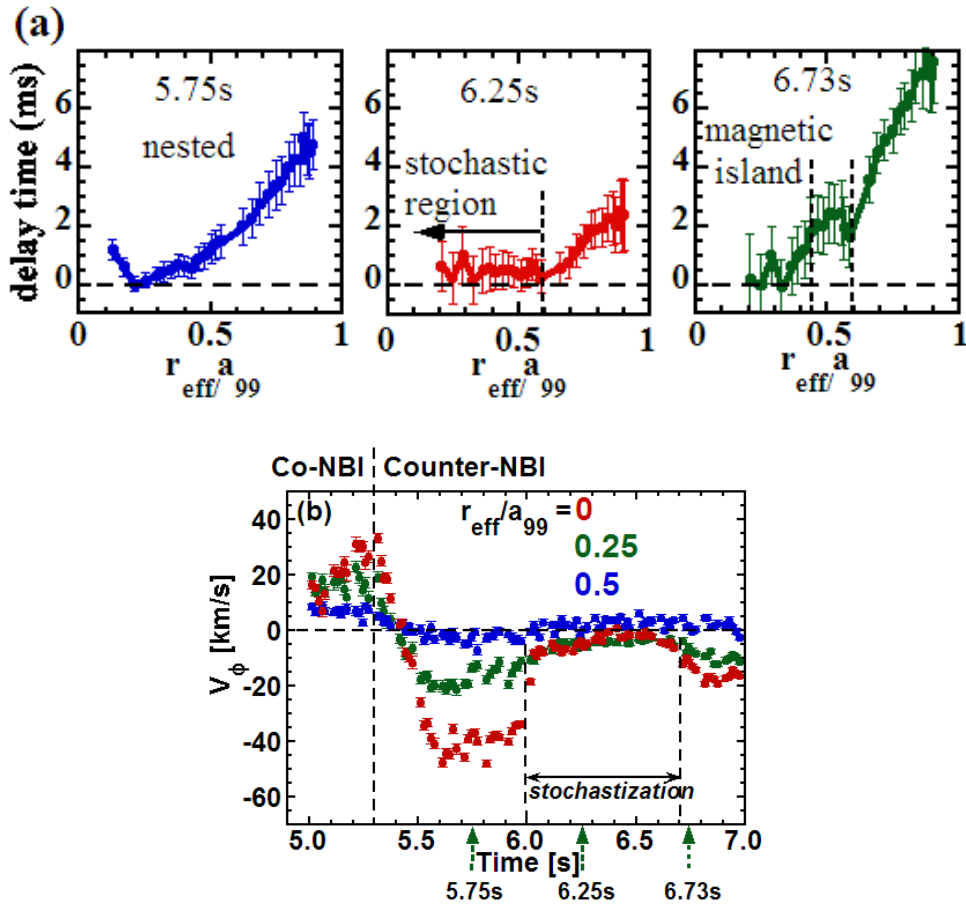
14

FIG.8. (a) Radial profiles of the delay time of heat pulse produced by MECH at three timings, and (b) toroidal flow velocity measured by MSE at three radial positions with three timings in (a) clearly indicated.

New excitation phenomenon of a geodesic acoustic mode (GAM) has been discovered through measuring the electric potential fluctuation and density fluctuation by a heavy ion beam probe (HIBP) [27], the poloidal magnetic field fluctuation by Mirnov coil array, and the energy distribution function of ions by a Neutral Particle Analyzer (NPA) [28]. Although the GAM is normally stable, it is abruptly excited with the time scale of approximately 1 ms when the chirping frequency of an energetic particle-driven GAM (EGAM) approaches twice the GAM frequency. The experimental results indicate the nonlinear growth of the abruptly excited GAM and the mode coupling between the GAM and the initially excited EGAM.

In order to interpret the abrupt phenomena, a model taking into account both kinetic nonlinearity and fluid nonlinearity has been proposed [29,30]. According to the model, the abrupt excitation phenomenon can be interpreted as a subcritical instability of the GAM. A simulation based on the model with experimental parameters successfully reproduces the time scale, the amplitude, and the timing of the excitation. Because a subcritical instability is a working hypothesis for understanding of the trigger problem of the abrupt phenomena, this observation in the LHD will show an experimental path to resolve the trigger problem. Recently, a simulation based on the first principle is being developed [31], and the direct comparison between the experiment and the simulation will give better understanding of the abrupt excitation phenomenon in the near future.

From the viewpoint of atomic physics, LHD can be regarded as a unique light source for spectroscopic studies on impurity ions because of wide parameter ranges, low opacity and high tolerance for the impurities. In addition, impurity pellet injection systems and reliable diagnostic tools are routinely available in LHD. Therefore, we have exploited LHD to produce an experimental database of extreme ultraviolet (EUV) spectra from a variety of heavy ions including tungsten, tin and lanthanides. Until now, we have systematically investigated more than half of the elements with atomic numbers higher than 50. For example, Figure 9 shows the measured temperature dependence of the EUV spectrum from terbium (Tb) ions, one of the candidates for the next-generation light sources for semiconductor lithography [32]. Thanks to the maximum capability to control the electron temperature in LHD, we could successfully observe the drastic change in the spectral feature from discrete to quasi-continuum as the temperature decreases. The discrete feature at the high temperature case (Figure 9 (a)) originates mainly from higher charge states around Cu-like, while the quasi-continuum features in the low temperature case (Figure 9 (b)) consist of contributions from lower charge states. The isolated lines at 7.203 and 8.796 nm in the high temperature case are identified as the transitions of Cu-like Tb36+ ions, which are found for the first time in LHD. In a similar way, we have identified some of the isolated lines from neodymium (Nd), holmium (Ho) and thulium (Tm) ions for the first time [33]. The experimental database developed in LHD will be helpful for verification of atomic models of tungsten emissions in ITER [34] as well as plasma light sources for industrial applications.
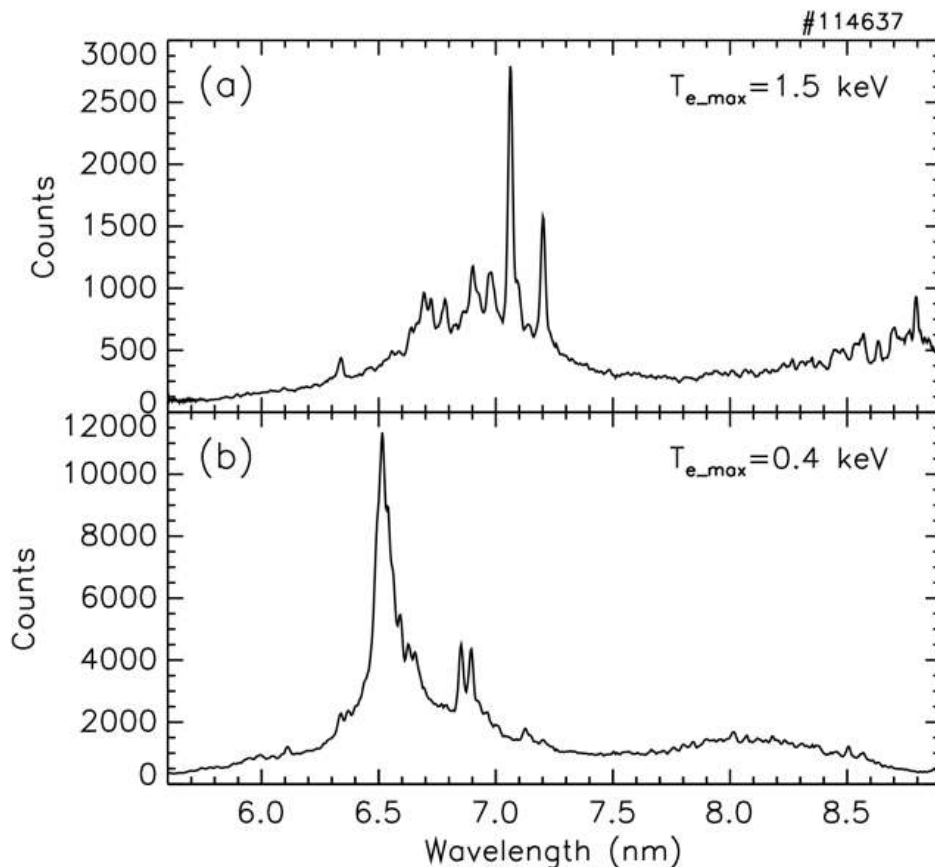

Figure 9: EUV spectra observed in (a) high and (b) low electron temperature discharges.

5. Summary

The deuterium experiment will start from March 2017. Before that, the finalization and summarization of the hydrogen experiment towards the deuterium phase were performed.

In the high beta trial, experiments with relatively high magnetic field of 1 T were performed, expecting the increase of T_e. The high $<\beta>$ regime around 4 % was extended to an order of magnitude lower collisional regime than before. In this situation, transition to the improved particle confinement mode was observed during the increase in $<\beta>$.

In the high temperature experiment, high ion and electron temperatures, T_i, T_e, of more than 6 keV were simultaneously achieved by superimposing the high power ECH on the NBI heated plasma. It is found that T_e and its gradient increased with increase of ECH power both in the plasma core and in the edge. On the other hand, the T_i gradient decreased in the plasma core with increase in the ECH power. However, core T_i can be increased by on-axis ECH, if n_e is high. This feature is quite beneficial for the high T_i scenario in high density plasmas such as DEMO, where electron heating is dominant.

Impurity behaviour in hydrogen discharges with NBI heating was classified with the plasma parameters (n_e, T_e) at the LCFS. It was found that there exists no impurity accumulation regime where the high performance plasma is maintained with high power heating ($P_{NBI} > 10$ MW), which is favourable for realizing fusion plasmas. Wide parameter scan experiments suggest that the toroidal rotation and the turbulence are the candidates to exhaust impurities from the core region. In the edge stochastic region, impurity flow properties experimentally obtained agree well with those obtained in theoretical modelling. This result suggests that the impurity parallel flow is mainly determined by the momentum balance along the magnetic field line.

Global particle balance was studied. It was found that there exists dynamic change of the helium wall retention. The inventory can mainly be separated into three phases. In the first phase, quite high wall inventory occurs. After the first phase, the wall inventory shows modest declination. However, the high wall inventory appears again in the third phase. The physics of the phased retention can be discussed based on a simple assumption that there are two kinds of helium reservoir, "first wall with stainless" and "divertor plate with graphite".

Based on the results in the hydrogen experiment mentioned above, LHD is about to enter the next stage. In the deuterium experiment, high-performance plasmas through confinement improvement are expected, which promote the scientific research in more reactor-relevant conditions. In addition, clarification of the isotope effect on confinement is also an important theme, since it has been a long-standing mystery in fusion research. Physics understanding is crucially important to accurately predict the behavior of the burning plasma. Demonstration of the confinement capability of energetic ions is also a crucial issue for LHD to promote reactor studies in helical devices.

17

References

[1]   Iiyoshi A. *et al* 1999 Overview of the Large Helical Device Project, *Nucl. Fusion* **39** 1245

[2]   Nagaoka K. *et al* 2015 Integrated discharge scenario for high-temperature helical plasma in LHD, *Nucl. Fusion* **55** 113020

[3]   Morisaki T. *et al* 2007 Superdense core mode in the large helical device with an internal diffusion barrier *Phys. Plasmas* **14** 056113

[4]   Komori A. *et al* 2010 Goal and Achievements of Large Helical Device Project, *Fusion Science and Technology* **58** 1

[5]   Kasahara H. *et al*, "Progress of High-Performance Steady-State Plasma and Critical PWI Issue in LHD". Preprint: 2014 IAEA Fusion Energy Conference, St. Petersburg IAEA-CN-221

[6]   Ida K. *et al* 2015 Overview of transport and MHD stability study: focusing on the impact of magnetic field topology in the Large Helical Device *Nucl. Fusion* **55** 104018

[7]   Kobayashi M. *et al* 2013 Control of 3D edge radiation structure with resonant magnetic perturbation fields applied to the stochastic layer and stabilization of radiative divertor plasma in LHD, *Nucl. Fusion* **53** 093032

[8]   Motojima O. *et al* 1999 Initial physics achievements of large helical device experiments *Phys. Plasmas* **6** 1843

[9]   Sakakibara S. *et al* 2017 Extension of High-beta Plasma Operation to low collisional Regime *Nucl. Fusion* **57** 066007

[10]   Funaba H. *et al* 2010 Local transport property of high-beta plasmas on LHD *Fusion Sci. Technol.* **58** 141

[11]   Sakakibara S. *et al* 2010 Study of MHD Stability in LHD *Fusion Sci. Technol.* **58** 176

[12]   Takahashi H. *et al* 2017 Extension of Operational Regime in High-Temperature Plasmas and Effect of ECRH on Ion Thermal Transport in the LHD *Nucl. Fusion* **57** 086029

[13]   Tsujimura T. *et al* 2015 Development and application of a ray-tracing code integrating with 3D equilibrium mapping in LHD ECH experiments *Nucl. Fusion* **55** 123019

[14]   Nakamura Y. *et al* 2017 Strong Suppression of Impurity Accumulation in Steady-State Hydrogen Discharges with High Power NBI Heating on LHD *Nucl. Fusion* **57** 056003

[15]   Nakamura Y. *et al* 2014 Impurity shielding criteria for steady state hydrogen plasmas in the LHD, a heliotron-type device *Plasma Phys. Control. Fusion* **56** 075014

[16]   McCormick K. *et al* 2002 New Advanced Operational Regime on the W7-AS Stellarator *Phys. Rev. Lett.* **89** 15001

[17]   Grigull P. *et al* 2003 Divertor operation in stellarators: results from W7-AS and implications for future devices *Fusion Eng. Des.* **66-68** 49

[18]   Kobayashi M. 2015 3D effects of edge magnetic field configuration on divertor/scrape-off layer transport and optimization possibilities for a future reactor *Nucl. Fusion* **55** 104021

[19] Oishi T. *et al* "Observation of Carbon Impurity Flow in the Edge Stochastic Magnetic Field Layer of Large Helical Device and its Impact on the Edge Impurity Control", submitted to Nucl Fusion.

[20] Oishi T. *et al* 2014 Space-resolved 3 m normal incidence spectrometer for edge impurity diagnostics in the large helical device *Appl. Opt.* **53** 6900

[21] Motojima G. *et al* "Global particle balance and its relationship with the plasma wall interaction emerging in long pulse discharges on the Large Helical Device", submitted to Nucl Fusion (NF-101858)

[22] Motojima G. *et al* 2015 Global helium particle balance in LHD *J. Nucl. Mater.* **463** 1080

[23] Ida K. *et al* 2015 Flow damping due to stochastization of the magnetic field *Nat. Commun.* **6** 6816

[24] Ida K. *et al* 2013 Topology bifurcation of a magnetic flux surface in magnetized plasmas *New J. Phys.* **15** 013061

[25] Ida K. *et al* 2010 Measurement of rotational transform with motional stark effect spectroscopy *Fusion Sc. Technol.* **58** 383

[26] Yoshimura M. *et al* 2010 Charge-exchange spectroscopy with pitch-controlled double-slit fiber bundle on LHD *Fusion Sci. Technol.* **58** 375

[27] Ido T. *et al* 2010 Development of 6-MeV heavy ion beam probe on LHD *Fusion Sci. Technol.* **58** 436

[28] Ido T. *et al* 2016 Strong Destabilization of Stable Modes with a Half-Frequency Associated with Chirping Geodesic Acoustic Modes in the Large Helical Device *Phys. Rev. Lett.* **116** 015002

[29] Lesur M. *et al* 2016 Nonlinear Excitation of Subcritical Instabilities in a Toroidal Plasma *Phys. Rev. Lett.* **116** 015003

[30] Itoh K. *et al* 2016 Onset condition of the subcritical geodesic acoustic mode instability in the presence of energetic-particle-driven geodesic acoustic mode *Plasma Physics Reports* **42** 428

[31] Wang H. *et al*, "Simulations of Energetic Particle Driven Geodesic Acoustic Mode and Global Alfvén Eigenmode in 3D LHD Equilibrium". Preprint: 2016 IAEA Fusion Energy Conference, Kyoto IAEA-CN-234-0565

[32] Suzuki C. *et al* 2015 Temperature dependent EUV spectra of Gd, Tb and Dy ions observed in the Large Helical Device *J. Phys. B: At. Mol. Opt. Phys.* **48** 144012

[33] Suzuki C. *et al* 2017 Extreme ultraviolet spectroscopy and atomic models of highly charged heavy ions in the Large Helical Device *Plasma Phys. Control. Fusion* **59** 014009

[34] Murakami I. *et al* 2015 Development of quantitative atomic modeling for tungsten transport study using LHD plasma with tungsten pellet injection *Nucl. Fusion* **55** 093016